AIAA Journal, Volume 62, Issue 1, January 2024, pp. 79-91
DOI:10.2514/1.J063209

Characteristics of shock-induced boundary layer separation on nacelles under windmilling diversion conditions*

Luca Boscagli†, David MacManus‡ and Fernando Tejero§
Centre for Propulsion Engineering, Cranfield University, Cranfield, MK43 0AL, UK

Kshitij Sabnis¶ and H. Babinsky‖
Department of Engineering, University of Cambridge, Cambridge, CB2 1PZ, UK

Christopher T. Sheaf**
Installation Aerodynamics, Rolls-Royce plc, Derby, DE24 8BJ, UK

The boundary layer on the external cowl of an aero-engine nacelle under windmilling diversion conditions is subjected to a notable adverse pressure gradient due to the interaction with a near-normal shock wave. Within the context of Computational Fluid Dynamics (CFD) methods, the correct representation of the characteristics of the boundary layer is a major challenge to capture the onset of the separation. This is important for the aerodynamic design of the nacelle as it may assist in the characterization of candidate designs. This work uses experimental data obtained from a quasi-2D rig configuration to provide an assessment of the CFD methods typically used within an industrial context. A range of operating conditions is investigated to assess the sensitivity of the boundary layer to changes in inlet Mach number and mass flow through a notional windmilling engine. Fully turbulent and transitional boundary layer computations are used to determine the characteristics of the boundary layer and the interaction with the shock on the nacelle cowl. The correlation between the onset of shock induced boundary layer separation and pre-shock Mach number is assessed and it was found that the CFD is able to discern the onset of boundary layer separation.

Nomenclature

C_f = Skin friction coefficient [−]

H = Shape factor [−]

$I_{\overline{U}}$ = Turbulence intensity magnitude [%]

*This is a modified version of our conference paper no. 2023-3384, AIAA Aviation Forum, 12-16th June 2023, San Diego, California
†Research Fellow, Centre for Propulsion Engineering, Cranfield University.
‡Professor of Propulsion Aerodynamics, Centre for Propulsion Engineering, Cranfield University.
§Lecturer in Propulsion Systems Design, Centre for Propulsion Engineering, Cranfield University.
¶Research Associate, Department of Engineering, University of Cambridge.
‖Professor of Aerodynamics, Department of Engineering, University of Cambridge, AIAA Fellow.
**Installation Aerodynamics Specialist, Installation Aerodynamics, Rolls-Royce plc.

L_{nac} = Axial distance between the nacelle highlight and trailing edge $[m]$

P_0, P = Total and static pressure $[Pa]$

S = Modulus of the mean rate-of-strain tensor $[1/s^2]$

s = Curvilinear coordinate along the nacelle aeroline $[m]$

T_0, T = Total and static temperature $[K]$

TKE = Modelled turbulent kinetic energy $[J/kg]$

U_e = Outer edge velocity of the boundary layer $[m/s]$

V_x = Axial velocity $[m/s]$

Δx = Local axial distance from the nacelle highlight $[m]$

Δx_{rig} = Axial extent of the rig $[m]$

y_{wall} = Wall distance $[mm]$

$\Delta y_{rig,in}$ = Height of the rig at the entry of the working section $[m]$

Δz_{rig} = Spanwise extent of the rig $[m]$

Greek symbols

β = Rotta-Clauser parameter $[-]$

δ = Boundary layer thickness $[mm]$

δ^* = Boundary layer displacement thickness $[mm]$

ρ = Flow density $[kg/m^3]$

ν = Kinematic viscosity $[m^2/s]$

ν_t = Eddy viscosity $[m^2/s]$

τ_x = Axial wall shear stress $[Pa]$

Subscripts

c = compressible

e = outer edge of the boundary layer

hi = nacelle highlight

i = incompressible

in = inlet of CFD domain

pre-sw = pre-shock-wave

Superscripts

+ = wall units

I. Introduction

The aerodynamic design of aero-engine nacelles has to fulfil both design and off-design operating conditions. Windmilling is an off-design condition which can arise when an engine is inoperative. Under these conditions the ingested mass flow reduces significantly [1] and the boundary layer on the external cowl of the nacelle could separate [2]. This could potentially lead to either a reduction in the aircraft flight envelope capability or an increase in thrust requirements on the operative engine. From a nacelle designer perspective, it is important to correctly capture the characteristics of the boundary layer and the onset of separation. Some of the current Computational Fluid Dynamics (CFD) methods used within an industrial context are challenged by the complex flow characteristics under these off-design conditions. Under windmilling diversion conditions [3–5], the flow undergoes a local supersonic expansion around the nacelle lip and forebody that terminates with a shock wave which interacts with the boundary layer. The favourable pressure gradient around the nacelle leading edge can also induce boundary layer relaminarization that can adversely affect the interaction with the shock.

Most of the turbulence models typically used along with Reynolds Averaged Navier Stokes (RANS) equations in an industrial context are insensitive to laminarization and curvature [6]. Moreover, RANS based methods quite often fail to predict boundary layer reattachment due to the insufficient production of turbulent kinetic energy within the shear layer [7]. Eddy resolving methods such as Large Eddy Simulations (LES) and hybrid RANS-LES methods can overcome some of the RANS deficiencies [6] but they are still computationally prohibitive within an industrial design optimisation framework. Thus, there is a need for high quality experimental data that can enable the evaluation and calibration of the RANS-based CFD methods. A recent experimental campaign using a quasi-2D rig representative of the aerodynamics of an aero-engine nacelle under windmilling diversion conditions (Fig. 1, [8, 9]) provides a dataset to determine the characteristics of the boundary layer on the nacelle cowl and the interaction with the shock wave. A similar arrangement of the rig was previously used to investigate Shock-wave Boundary Layer Interaction (SBLI) on a configuration representative of an intake at high-incidence [10, 11]. A new configuration for windmilling diversion conditions was developed which also included optical access for schlieren and Laser Doppler Anemometry (LDA) measurements (Fig. 1).

The rig for the windmilling diversion configuration was made of upper and lower liners that were representative of two streamlines inside and outside the engine captured streamtube, respectively. The position of the nacelle aeroline within the rig subdivided the main channel into an upper and lower bifurcation (Fig. 2). The boundary layer on a 3D-annular nacelle under windmilling conditions is sensitive to minor changes in the mass flow through the inoperative engine [4]. Mass Flow Capture Ratio ($MFCR = \frac{A_\infty}{A_{hi}}$) is a non-dimensional parameter that is typically used to describe the size of area of the ingested streamtube at nacelle highlight (A_{hi}) relative to the area far upstream from the engine (A_∞). Thus, the rig was designed to achieve both attached and separated conditions of the boundary layer on the nacelle cowl due to the interaction with the shock. The latter was achieved either through a change in inlet Mach

number (M_{in}) or through interchangeable bump geometries to mimic a change in the $MFCR$ via a change in mass flow split between upper and lower channel of the rig. Changes in mass flow split caused a change in the location of the stagnation point further into the upper side of the nacelle aeroline. The range of MFCR and M_{in} were determined based on 3D CFD studies of full-size engine nacelles where the boundary layer on the external cowl moved from attached to separated conditions due to the interaction with the shock. Thus, the sensitivity of the Shock-wave Boundary Layer Interaction (SBLI, Fig. 2) to changes either in M_{in} or $MFCR$ was evaluated within the experiments and this is sufficiently representative of the aerodynamic characteristics of a full-engine size 3D-annular nacelle. Overall, this work uses experimental data to provide an evaluation of RANS based methods and determine the limits of the turbulence models typically used within the aerodynamic design optimisation of aero-engine nacelles within industrial settings [4, 5, 12].

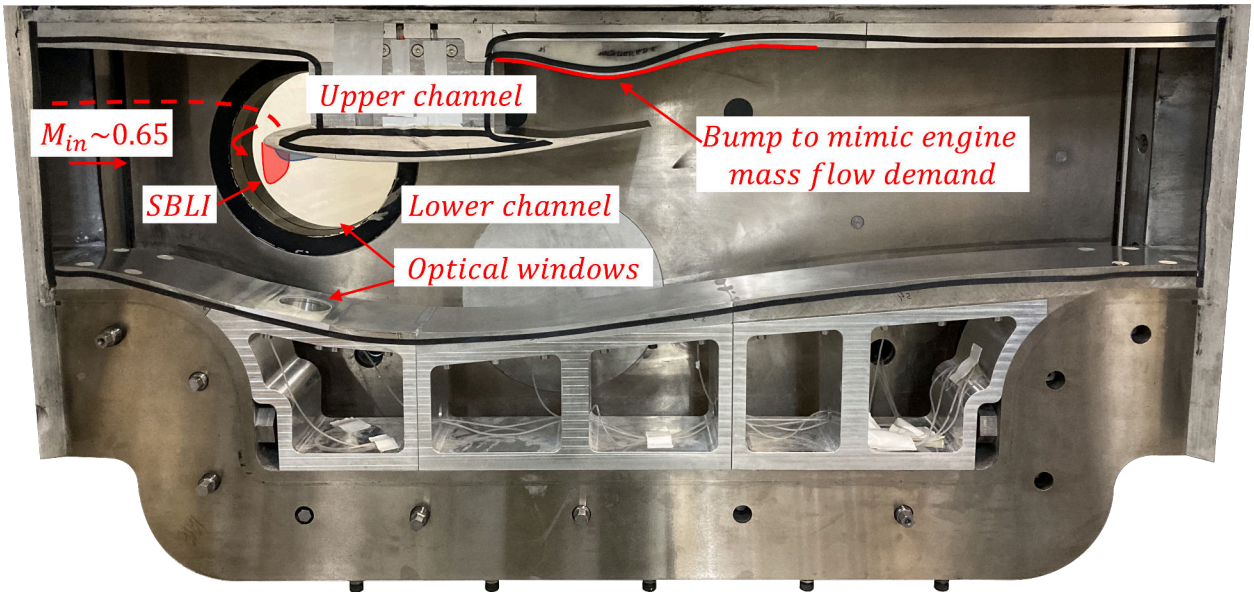

Fig. 1 Lateral view of the rig configuration for the windmilling diversion studies

II. Methodology

A. Computational methods

For the CFD computations a double-precision density based solver with an implicit time integration formulation [13] was used. A Roe scheme was used for the computation of the numerical fluxes and it was based on a Green-Gauss method for the spatial discretization. Reynolds Averaged Navier Stokes (RANS) equations were solved and the $k\omega - SST$ [14] and $\gamma - Re_\theta$ [15] were used for fully turbulent and transitional computations, respectively. A polytropic ideal gas model was used for the air and the viscosity was computed based on Sutherland's law. All the wind tunnel walls were modelled including the holding-plates (Fig. 2) which are used to retain the nacelle section as well as to adjust the

nacelle incidence angle. For the computational domain, the upper and lower walls of the rig were axially extruded at the entry and at the exit of the working section for about twice the height of the rig inlet ($\Delta y_{in,rig}$) for numerical stability reasons. The bounding walls were modelled as adiabatic viscous walls apart from an inviscid section at the inlet of the CFD domain that was used to ensure to reproduce the thickness of the boundary layer, which was measured at the entry of the working section ($\delta|_{x=0}$, Table 1 and Fig. 2). Total pressure ($P_{0,in}$), temperature ($T_{0,in}$) and turbulence intensity ($I_{\overline{U}}$) were prescribed at the inlet of the CFD domain. The turbulence intensity was the same as measured within the rig and a turbulent viscosity ratio $\nu_t/\nu = 10$ was used. The static pressure at the outlet of the CFD domain was varied to achieve the experimental Mach number at the entry of the working section (M_{in}). This was inferred from the value of the static pressure measured through a static pressure tap on the side-walls of the rig, located approximately at the tunnel mid-height and $0.09\Delta y_{in,rig}$ downstream of the entry of the working section. At that axial position within the rig, the flow significantly accelerates closer to the lower section due to the notable streamwise curvature of the rig wall. This contributed to a non-uniform isentropic Mach number (M_{ise}, Eq. 1) distribution on the side-wall, with an overall variation of about $\Delta M_{ise} \approx 0.2$. Nevertheless, at the probe height ($y/\Delta y_{rig,in} \approx -0.48$) the isentropic Mach number closely matched the nominal inlet Mach number ($M_{in} = 0.65$). Furthermore, the correspondence of the thickness of the boundary layer at the entry of the working section between the CFD and the experiments ensured that the inlet Mach number inferred from the measurement of the static pressure at the rig side-wall was sufficiently representative of the nominal conditions.

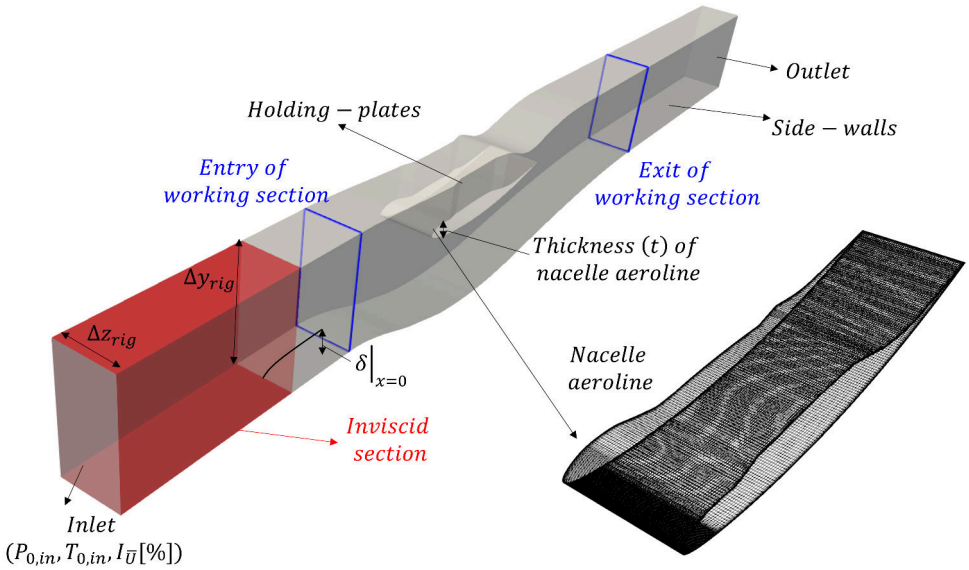

Fig. 2 Schematic of the CFD domain and grid refinement on the nacelle aeroline

$$M_{ise} = \sqrt{\frac{2}{\gamma - 1}\left[\left(\frac{P_{0,in}}{P}\right)^{\frac{\gamma-1}{\gamma}} - 1\right]} \tag{1}$$

Table 1 Nominal operating point of the rig

	M_{in} **[-]**	Re_t $[\times 10^6]$	$\delta\|_{x=0}$ **[mm]**	$I_{\overline{U}}$ **[%]**
Diversion	0.65	1.05	2-3	0.6

1. CFD data analysis

Around the nacelle leading edge, the boundary layer undergoes a supersonic expansion that can potentially induce relaminarization [16, 17]. The acceleration of the flow within the boundary layer region was quantified based on an acceleration parameter (K,[18]) that was computed as described in Eq. 2,

$$K = \frac{\nu}{U_{in}^2} |\overrightarrow{\nabla}\mathbf{U} \cdot \hat{\tau}| \tag{2}$$

Where ν and U_{in} are the kinematic viscosity and the velocity at the inlet of the working section, respectively; $\overrightarrow{\nabla}\mathbf{U}$ is the velocity gradient tensor and $\hat{\tau}$ is the local unitary vector parallel to the nacelle wall. Typically, the flow is likely to relaminarize for $K > 3 \times 10^{-6}$ [19]. The production of modelled turbulent kinetic energy (G_k, Eq. 3) is also evaluated to understand how the peak and wall-normal distribution of post-shock G_k varies when either a transitional or fully turbulent SBLI is modelled. After the initial supersonic expansion, which terminates with a near-normal shock wave, the flow decelerates under the influence of an adverse pressure gradient ($\partial P/\partial x > 0$). The Rotta-Clauser [20] parameter (β, Eq. 4) is typically used to quantify the amount of diffusion that the boundary layer is subjected to and, for an equilibrium turbulent boundary layer, β is constant along the streamwise direction [21]. In Eq. 4, $\overrightarrow{\nabla} p_e$ is the pressure gradient evaluated at the outer edge of the boundary layer, δ_i^* is the incompressible displacement thickness and τ_w is the magnitude of the wall shear stress.

$$G_k = \frac{\nu_t}{\rho} S^2 \tag{3}$$

$$\beta = \frac{\delta_i^*}{\tau_w} \overrightarrow{\nabla} p_e \cdot \hat{\tau} \tag{4}$$

Although the outer flow is not necessarily irrotational due to the entropy gradient across the shock, for the CFD results a threshold based on the magnitude of the vorticity (ϵ) was used to determine the outer edge of the boundary layer (Eq. 5). Ahead of the shock and further downstream where the boundary layer starts to recover, the method is sufficiently robust to provide an estimate of the flow acceleration and of the mass flux and momentum deficit within the boundary layer. ϵ was progressively reduced from $\epsilon = 10^{-2}$ to 10^{-4} and the outer edge of the boundary layer was identified when a further reduction in ϵ did not affect the characteristics of the boundary layer. Unless differently specified, for all the results presented in this work, $\epsilon = 10^{-3}$ was used to determine the outer edge of the boundary layer and to

compute the associated integral quantities through a trapezoidal numerical integration rule. Both the compressible and the incompressible formulations [22, 23] were used to determine the integral characteristics of the boundary layer. Despite the compressible regime, the incompressible formulation is justified by the fact that typically within experiments the local value of the density of the flow is not available. Furthermore, based on the Morkovin's hypothesis [24], the compressibility effects on the characteristics of the boundary layer may be negligible for a Mach number below 5.

$$U = U_e \Leftrightarrow \frac{|\overrightarrow{\omega}_e|}{|\overrightarrow{\omega}_{y_{wall}=0}|} \leq \epsilon \tag{5}$$

The characteristics of the shock were determined based on peak isentropic Mach number as well as shock strength (i.e., static pressure rise, $PR_{sw} = P_{post,sw}/P_{pre,sw}$) and interaction length (L_{sw}, Fig. 3a). Following a similar approach to the one used by Coschignano and Babinsky (2019) [11], the pre-shock pressure ratio ($P_{pre,sw}/P_{0,in}$) was determined based on the second derivative of the static pressure ($\frac{\partial^2 P}{\partial x^2}$), a few grid points ahead of the maximum $\frac{\partial^2 P}{\partial x^2}$ (Fig. 3b). The post-shock location corresponded to the sonic pressure ratio ($P_{post,sw}/P_{0,in} \approx 0.528$).

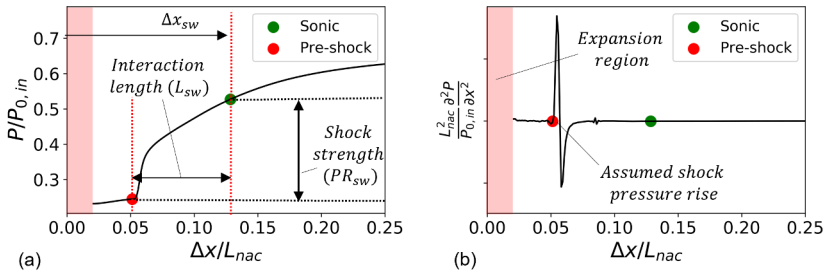

Fig. 3 Schematic of the definition of shock strength and interaction length

2. Grid refinement studies

A grid independence study [25] was carried out at the nominal operating conditions of the rig (Table 1) for a configuration with notable boundary layer separation on the nacelle aeroline. Three grid refinements were used and referred to as level 1, 2 and 3, respectively (Table 2). The resolution within the boundary layer was kept approximately the same through the grids with a $y^+ \approx 1$ and a cell growth ratio of 1.2. Compared to levels 2 and 3, level 1 grid significantly overestimated the spanwise extent of the corner flows (Fig. 4). The spanwise distribution of the separated region was only slightly different for level 2 and level 3 grids. The Grid Convergence Index (GCI) for level 2 grid relative to level 3 was 0.08%, 0.87% and 0.11% when computed based on the peak and pre-shock isentropic Mach number, and axial shock position on the nacelle aeroline at mid-span ($\Delta z = 0$), respectively. Relative to grid level 3, the characteristics of the boundary layer on the nacelle cowl at mid-span for level 2 were only slightly affected by the changes in outer grid resolution (Fig. 5). Overall, the differences between level 2 and level 3 grid were attributed to a slightly

different prediction of the corner flows. RANS methods based on linear eddy viscosity models are typically unable to correctly model corner secondary flows [26] due to the notable flow anisotropy that characterizes them [27, 28]. Nevertheless, a comprehensive analysis of the limitations of numerical models for corner flows is out of the scope of this work, which is focused on the assessment of the RANS methods for the prediction of the quasi-2D transonic shock-induced separation at mid-span. Thus, level 2 grid was considered sufficiently grid independent and the same spanwise, streamwise and wall-normal resolutions (Table 2) were used for the subsequent studies.

Table 2 Overall grid size and average resolution around the nacelle aeroline

Grid level	**Number of nodes** [$\times 10^6$]	$\Delta x/\Delta z_{rig}$[%]	$\Delta y/\Delta z_{rig}$[%]	$\Delta z/\Delta z_{rig}$[%]	y^+
1	2.4	2	1.6	2.2	1
2	5.5	1.5	1.35	1.25	1
3	15	1.1	1.15	0.625	1

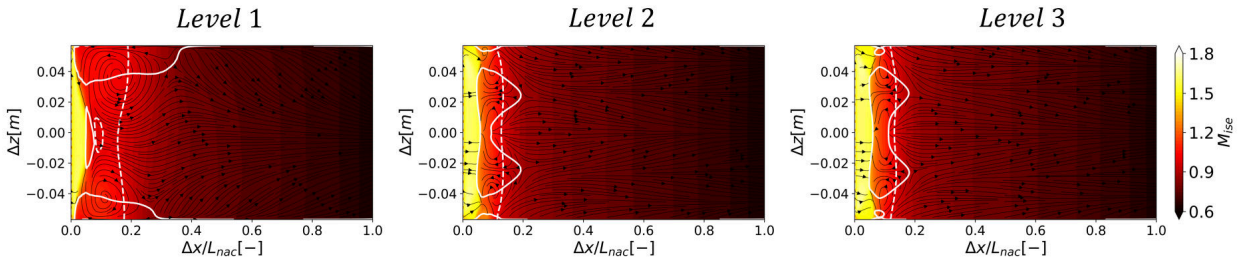

Fig. 4 Grid resolution studies. White solid line: $\tau_{w,x} = 0$; white dashed line: $M_{ise} = 1$. RANS computations with $k\omega - SST$

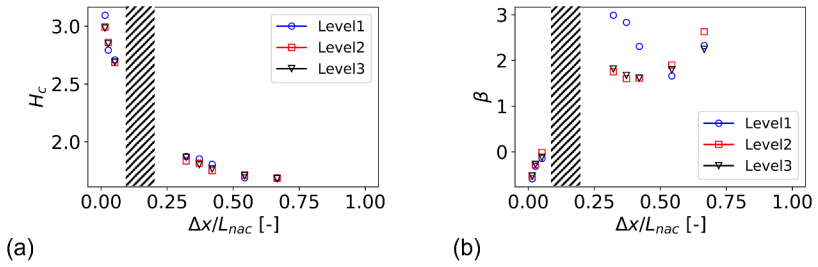

Fig. 5 Effect of grid resolution on boundary layer characteristics on the nacelle aeroline at $\Delta z = 0$. RANS computations with $k\omega - SST$

3. Turbulence model assessment

Fully turbulent steady RANS computations with Spalart-Allmaras (SA, [29]) and $k\omega - SST$ were used to assess the impact of the turbulence model on the separation onset of the boundary layer on the nacelle cowl. At the nominal rig operating conditions (Table 1), the mass flow through the upper bifurcation of the rig was reduced to promote

shock-induced separation on the nacelle cowl through an increase in the bump height ($h_{bump,2}$) relative to a reference attached condition ($h_{bump,1}$). For both cases the isentropic Mach number distribution and separation extent on the nacelle at mid-span ($\Delta z = 0$) was similar (Fig. 6a,b) for the two turbulence model with the peak isentropic Mach number that was about 0.02 greater for SA compared to $k\omega - SST$ at the conditions with boundary layer separation ($h_{bump,2}$). Furthermore, the position of stagnation point was the same for the two turbulence models (Fig. 6c), which indicated a similar mass flow split through the rig. Thus, the separation onset of the boundary layer was sufficiently independent of the choice of the turbulence model and the $k\omega - SST$ turbulence model was used for the subsequent studies as this is also typically used for the design and optimisation of aero-engine nacelles [12, 30].

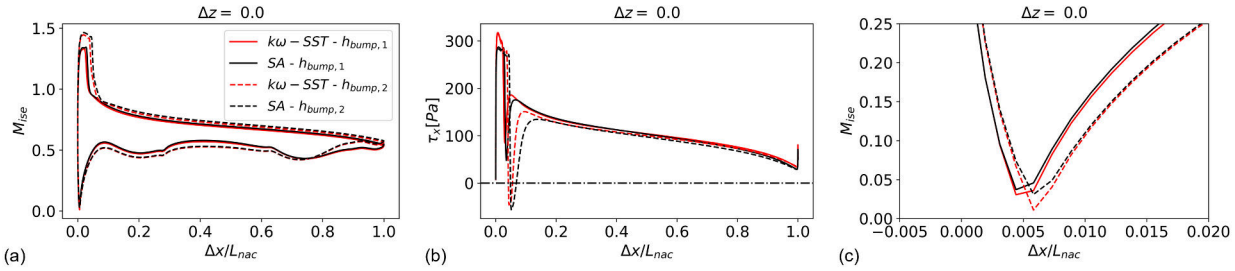

Fig. 6 Effect of turbulence model on a) M_{ise}, b) τ_x distributions and c) position of the stagnation point on the nacelle cowl at $\Delta z = 0$

B. Experimental methods

The rig facility at the University of Cambridge [11, 31] was configured to enable the assessment of the characteristics of the separation of the boundary layer over a nacelle under windmilling diversion conditions (Table 1). A number of experimental techniques were used within the rig to characterize the flow field around the nacelle in terms of boundary layer status and characteristics, shock topology and strength, and extent of the corner flows. Conventional instrumentation, such as static pressure taps and oil flow visualization, was used alongside high-speed schlieren, Laser Doppler Anemometry (LDA), Pressure Sensitive Paint (PSP) and infrared thermography. The static pressure taps were connected to a differential pressure transducer. The error on the ratio between the static pressure and the inlet total pressure was approximately ±1% [32]. Relative to the isentropic Mach number, this approximately equates to an uncertainty that was below ±0.01 and ±0.07 around the shock and the stagnation point locations, respectively. However, for the latter the positional accuracy of the static pressure taps is more important, and this was approximately 0.075% of the nacelle length (L_{nac}). Error bars are sometimes omitted in the plots in the results section to improve the readability of the figures. Unless otherwise indicated, the marker size is approximately indicative of the uncertainty of the experimental measurements. For the schlieren visualizations, a Photron Fastcam Nova S6 camera was used at a frame rate of $6400 fps$ and an exposure time of $12\mu s$. The mean flow field was an average of approximately 2000 images. The LDA measurements were obtained on the nacelle aeroline at mid-span ($\Delta z = 0$) at three different axial

positions ($\Delta x/L_{nac} \approx 0.06$, 0.1 and 0.13, Fig. 7). Due to the finite size of the measurement volume, the positional accuracy of the LDA measurements normal to the wall was approximately $1/10^{th}$ of the local boundary layer thickness. The uncertainty on the local velocity measurement was typically about ±2%, and it increased to approximately ±20% closer to surface of the nacelle model [32]. The characteristics of the boundary layer ($I_{\overline{U}}$ and $\delta|_{x=0}$) were also measured at the entry of the working section to enable a correct representation of the effective inlet Mach number within the CFD model. A traverse Pitot probe and a single component hot-wire were used to measure the boundary layer thickness and streamwise turbulence intensity, respectively.

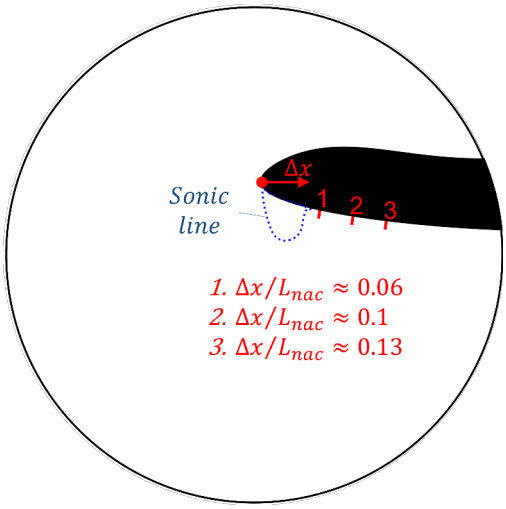

Fig. 7 Schematic of the axial position of the LDA measurement on the nacelle aeroline at mid-span ($\Delta z = 0$)

III. Results

Different CFD models were used to evaluate the accuracy of RANS based methods to predict the characteristics of boundary layer separation on nacelles under windmilling diversion conditions. Both qualitative and quantitative evaluation methods are used to determine the agreement between CFD and experiments. The validated CFD data are used to quantify the characteristics of the boundary layer ahead of the shock and to corroborate experimental findings.

A. Qualitative assessment

The effect of a change in mass flow split within the rig on the characteristics of the boundary layer on the nacelle aeroline was assessed through a series of interchangeable bump geometries (Fig. 8). The range of changes in mass flow split was selected to mimic the change in MFCR observed on a full-engine size 3D nacelle where the boundary layer on the external cowl also spans from attached to separated due to the interaction with the shock on the forebody. The different configurations were named with the ratio between the bump height (h_{bump}) and the height of the rig at the entry of the working section ($\Delta y_{rig,in}$). As the area on the upper channel was decreased, more flow went through the

lower channel and the stagnation point moved further downstream on the upper side of the nacelle aeroline. Thus, the acceleration length of the flow around the leading edge of the nacelle increased with a larger region of supersonic flow depicted by the bright region in the schlieren photographs in Fig. 9a.

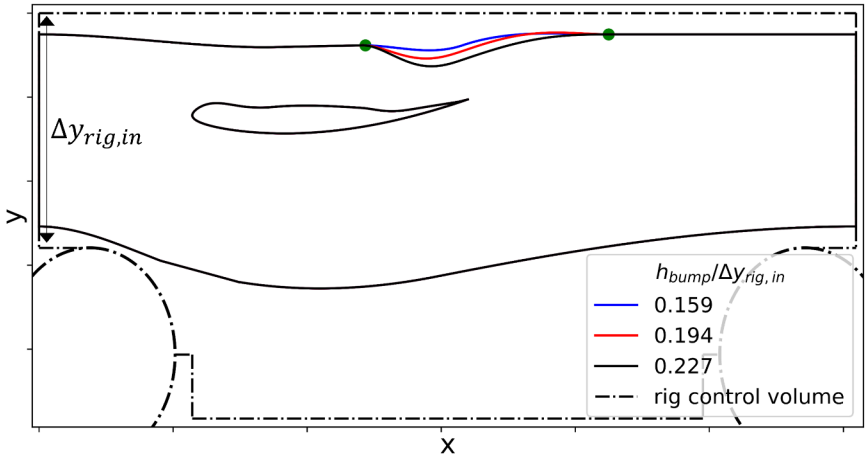

Fig. 8 Schematic of the rig configuration and bump geometries

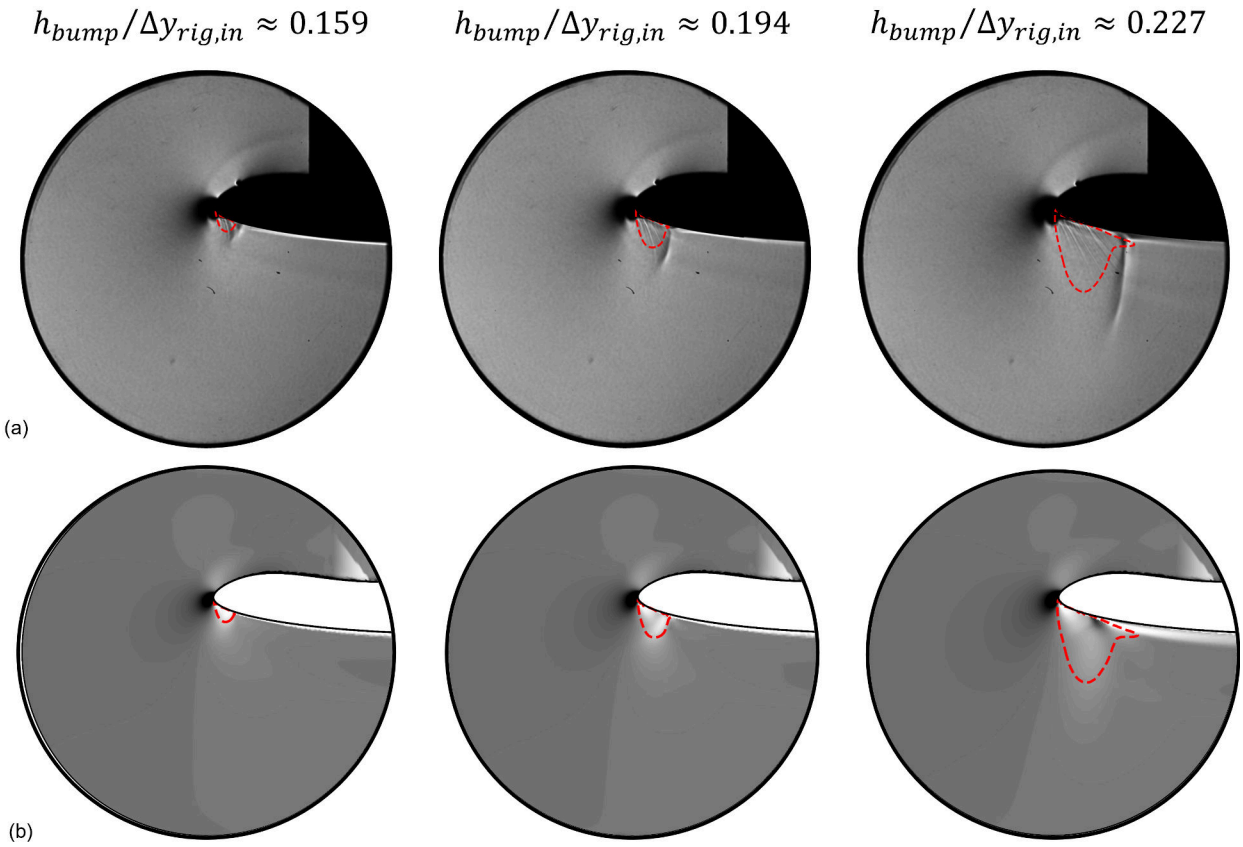

Fig. 9 a) Time-averaged schlieren photographs and b) spanwise averaged density gradient ($\partial\rho/\partial y$) of RANS with $k\omega - SST$; the red dashed line indicates the sonic line ($M = 1$) extracted from the CFD

The CFD results were spanwise averaged to enable a preliminary qualitative comparison of the predicted flow field with the schlieren photographs (Fig. 9). As the bump height increases, the boundary layer gets thicker and the supersonic region greater. The latter dictated an increase in pre-shock Mach number and shock strength that was sufficient to separate the boundary layer on the nacelle cowl. The separation of the boundary layer was detected in the experiments through the oil flow visualizations (Fig. 10a) and in the CFD based on the condition of negative axial wall shear stress ($\tau_{w,x} \leq 0$, Fig. 10b). For the configuration $h_{bump}/\Delta y_{in,rig} = 0.159$, both the CFD and the experiments had an attached flow field and the spanwise extent of the corner flows was less than 1% of the rig span (Δz_{rig}). As the bump height increases ($h_{bump}/\Delta y_{in,rig} = 0.194$), there was shock induced boundary layer separation both in the CFD predicted flow field and in the experiments. Sufficiently far away from the rig side-walls ($-0.04m \leq \Delta z \leq 0.04m$), the streamwise extent of the separation was almost independent of the spanwise location and therefore the influence of the corner flows on the SBLI at mid-span was negligible. Overall, for the configurations $h_{bump}/\Delta y_{rig,in} = 0.159$ and 0.194, there was good qualitative agreement between the CFD and the experiments in terms of shock location, extent of the supersonic region and of the boundary layer separation on the nacelle cowl (Fig. 9). On the other hand, there were significant differences for the configuration $h_{bump}/\Delta y_{rig,in} = 0.227$. The latter was associated to a considerably greater streamwise extent of the separated region in the CFD relative to the experiments. In the CFD, there was a notable spanwise variation of the separated region under the influence of the corner flows. Thus, it is argued that the lack of agreement between the CFD and the experiments for the configuration $h_{bump}/\Delta y_{rig,in} = 0.227$ may be due to the limitations of the turbulence model to correctly reproduce the secondary flows closer to the rig side-walls. In the following sections, the three rig configurations associated to the change in bump height are also referred to as 'attached', 'incipient separation' and 'well-established separation' cases to reflect the status (attached or separated) of the boundary layer on the external cowl of the nacelle and to ease the discussion around the three operating conditions.

B. Quantitative assessment

Static pressure taps and LDA measurements provide a quantitative assessment of the differences between CFD and experiments. Shock location and strength, and the position of the stagnation point were determined based on the static pressure on the nacelle aeroline at mid-span ($\Delta z = 0$). The static pressure taps were axially distributed at the rig mid-span ($\Delta z = 0$) and at two more slightly off-centered locations ($\Delta z = -4mm$ and $2mm$). For the configuration $h_{bump}/\Delta y_{rig,in} = 0.159$, the peak isentropic Mach number ($M_{ise,max}$) was about 1.3 with the shock located at about $0.03L_{nac}$ of the nacelle length from the leading edge (Fig. 11) and the boundary layer on the nacelle at mid-span was attached (Fig. 10). With about $0.04\Delta y_{rig,in}$ increase in bump height ($h_{bump}/\Delta y_{rig,in} = 0.194$), $M_{ise,max}$ increased to about 1.45 (Fig. 11) and the boundary layer separated (Fig. 10). For both configurations, there was generally good agreement between the CFD and the experiments with a difference in $M_{ise,max}$ and shock location below 0.02 and $0.005L_{nac}$, respectively. As anticipated in the previous section, the agreement between CFD and experiment

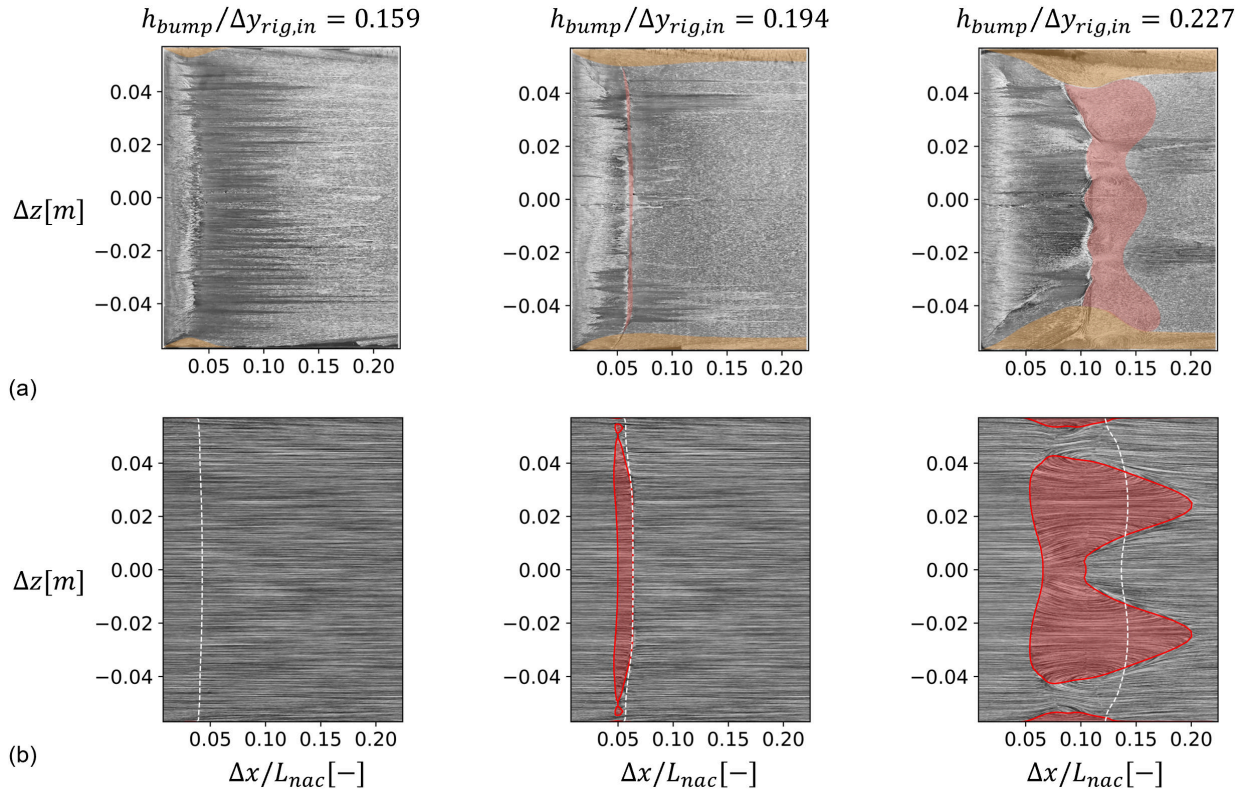

Fig. 10 a) Oil flow photographs (experiments) with corner flow (yellow) and boundary layer (red) separation highlighted (reproduced with permission from Sabnis et al. [32]). b) Line integral convolution [33] of wall shear stress vector field (RANS with $k\omega - SST$) on the nacelle aeroline; red shaded region: $\tau_{w,x} \leq 0$; white dashed line: $M_{ise} = 1$

deteriorated for the case $h_{bump}/\Delta y_{rig,in} = 0.227$. Despite a similar peak isentropic Mach number $M_{ise,max} \approx 1.6$, in the CFD the shock was about $0.02L_{nac}$ more upstream relative to the experiments (Fig. 11) and the streamwise extent of the separation across the rig span was significantly greater (Fig. 10). Also, the separated region in the CFD had a notable spanwise variation, whereas it was quite uniform in the experiments. The source of these differences is further investigated in the next paragraphs.

The agreement between CFD and experiments in the mass flow split was inferred from the static pressure axial distributions at mid-span ($\Delta z = 0$) on the upper and lower rig walls (Fig. 12). For example, for the configuration $h_{bump}/\Delta y_{rig,in} = 0.194$, the isentropic Mach number distributions on the upper and lower rig walls were similar, with the largest discrepancy being about $\Delta M_{ise} \approx 0.03$. This arose in the upper channel, where the flow slightly accelerates due to the reduction in area due to the holding-plates. The general good agreement in the M_{ise} distributions between CFD and experiments on the upper and lower walls indicated that the total pressure losses through the rig, hence the mass flow split, were similar. This confirmed the good agreement of the isentropic Mach number distribution around the stagnation point on the nacelle aeroline (Fig. 11). Thus, the slightly different shock location and pre-shock Mach number for CFD compared to the experiments may be associated to different characteristics of the boundary layer.

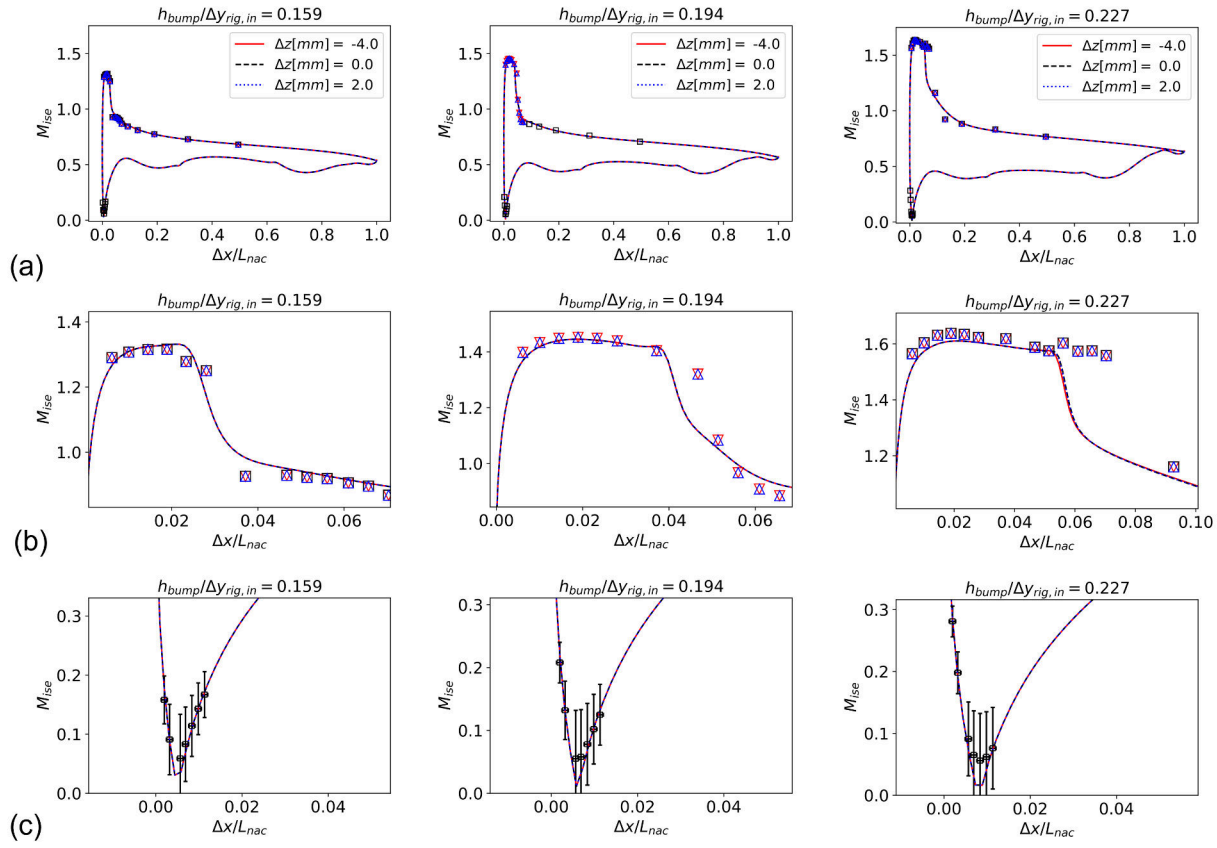

Fig. 11 Effect of bump height on M_{ise} distribution on the nacelle aeroline at $\Delta z = 0$. Lines: RANS computations with $k\omega - SST$; color-coded markers: experiments

The temperature distribution on the nacelle cowl obtained in the rig through infrared thermography showed that the interaction between the shock and the boundary layer was transitional [9]. The estimated recovery factor ahead of the shock was approximately 0.8, which is close to a theoretical value of 0.84 for a laminar boundary layer over a flat plate with zero pressure gradient [34] based on a Prandtl number for air of 0.71. Thus, the mismatch in the isentropic Mach number distribution between CFD and experiments was investigated through transitional boundary layer computations using the $\gamma - Re_\theta$ [15] turbulence model. The likely relaminarization of the turbulence model could also be inferred from the fully turbulent computations based on the acceleration parameter (K) ahead of the shock. For all the three bump configurations, K at about $0.015L_{nac}$ downstream of the highlight of the nacelle aeroline was up to 10-12 times greater than the typical [19] relaminarization threshold within the viscous sub-region of the boundary layer ($y^+ \leq 10$, Fig. 13).

For the configurations $h_{bump}/\Delta y_{rig,in} = 0.159$ and 0.194 at the nominal inlet Mach number ($M_{in} = 0.65$), the transitional boundary layer ($\gamma - Re_\theta$) computations improved the prediction of pre-shock Mach number ($M_{ise,pre-sw}$) and shock axial location (Δx_{sw}, Fig. 3). For example, for the attached case ($h_{bump}/\Delta y_{rig,in} = 0.159$), Δx_{sw} and $M_{ise,pre-sw}$ were about $0.028L_{nac}$ and 1.25 for both the experiments and the transitional ($\gamma - Re_\theta$) computations (Fig. 14), whereas the fully turbulent case ($k\omega - SST$) had $\Delta x_{sw} \approx 0.023L_{nac}$ and $M_{ise,pre-sw} \approx 1.35$ (Fig. 12). For the

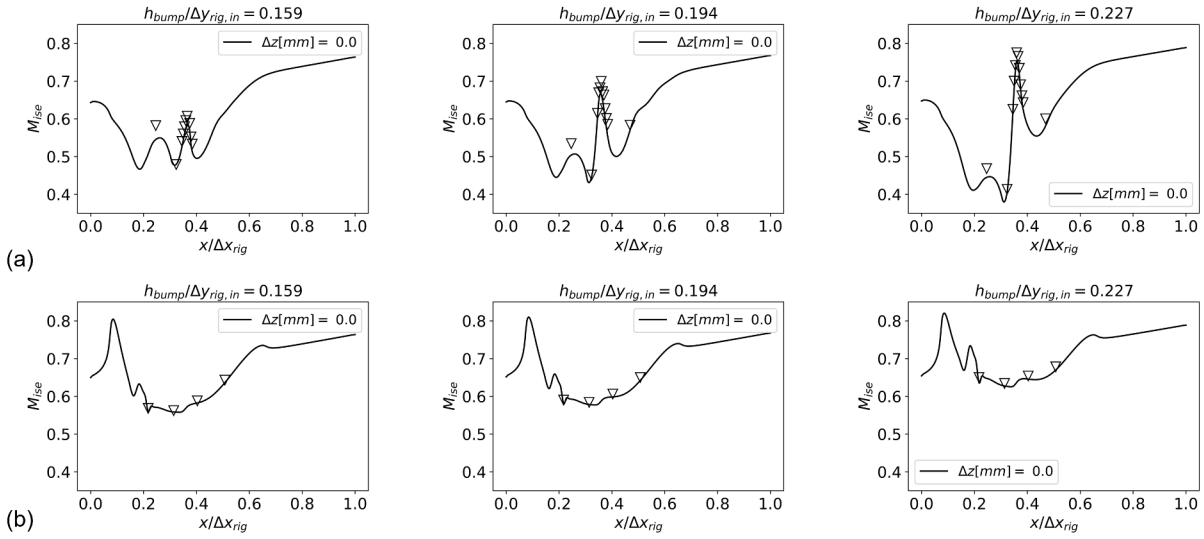

Fig. 12 Effect of bump height on M_{ise} distribution at mid-span ($\Delta z = 0$) on the a) upper and b) lower rig walls. Black solid line: RANS computations with $k\omega - SST$; markers: experiments

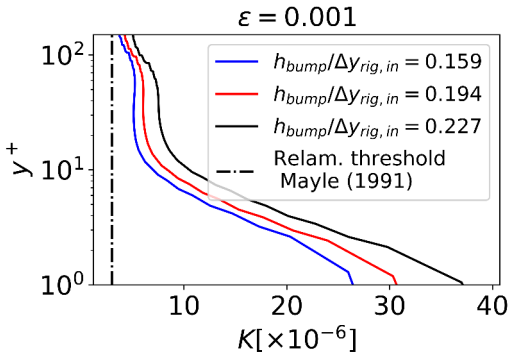

Fig. 13 Boundary layer acceleration on the nacelle aeroline at $\Delta z = 0$ ahead of the shock ($\Delta x/L_{nac} \approx 0.015$). $M_{in} = 0.65$; RANS computations with $k\omega - SST$

case with a well-established boundary layer separation ($h_{bump}/\Delta y_{rig,in} = 0.227$), both the transitional ($\gamma - Re_\theta$) and fully turbulent ($k\omega - SST$) computations had significantly different shock characteristics compared to the experiments. However, the topology of the corner flows was also notably different for the two turbulence models (Fig. 15), which may have contributed to a different spanwise distribution of the separated region. Although the maximum axial extent of the separated region was similar ($\approx 0.15L_{nac}$) between the models, for the fully turbulent case ($k\omega - SST$) the peak was off-centered relative to mid-span ($\Delta z \approx \pm 0.025m$), whereas it was quite uniform across the span for the transitional model ($\gamma - Re_\theta$). Overall, although for the attached and incipient separation case the $\gamma - Re_\theta$ model had a better agreement with the experiments relative to the M_{ise} distribution at mid-span, the evaluation of the boundary layer downstream of the shock is required to understand how the different shock topology (transitional or fully turbulent)

influences the reattachment point.

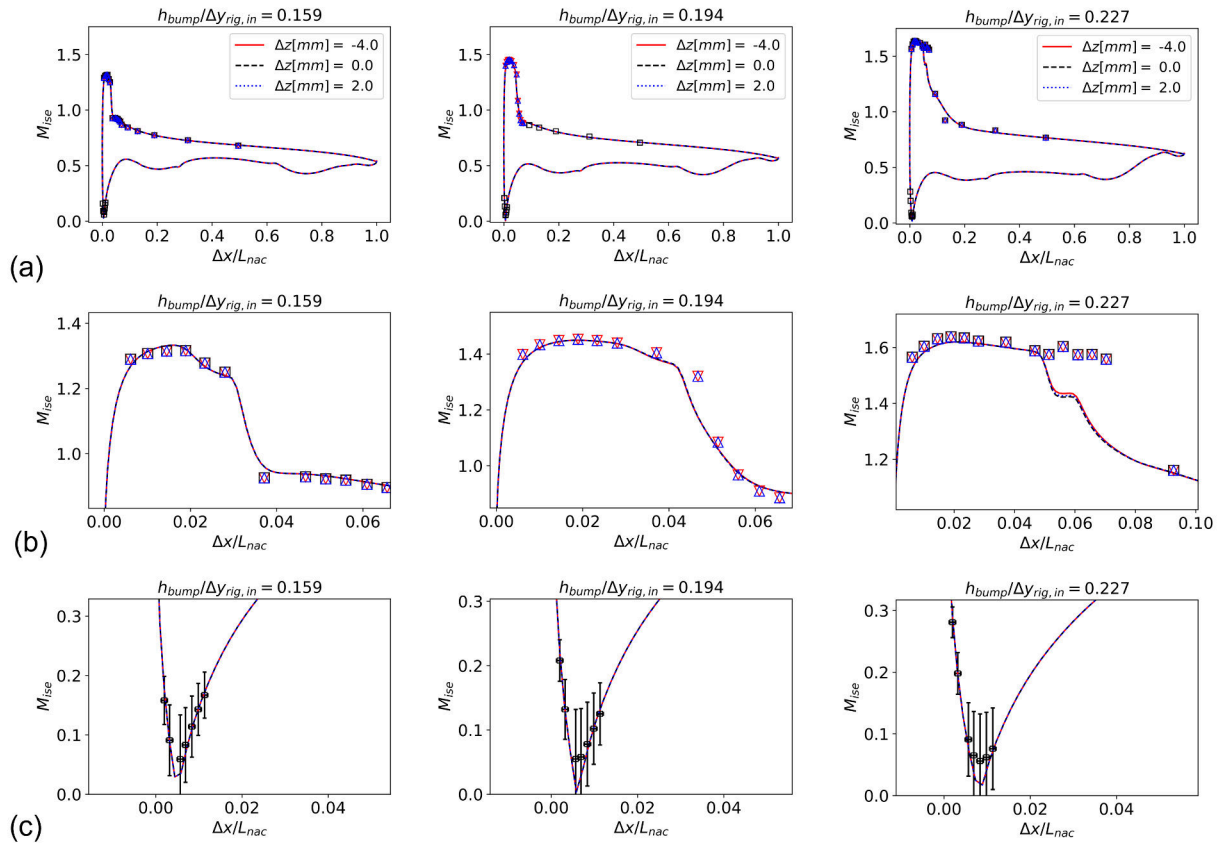

Fig. 14 Effect of bump height on M_{ise} distribution on the nacelle aeroline at $\Delta z = 0$. Lines: RANS computations with $\gamma - Re_\theta$; color-coded markers: experiments

Downstream of the shock ($\Delta x/L_{nac} \approx 0.06$), for the case with incipient separation ($h_{bump}/\Delta y_{rig,in} = 0.194$) both CFD models (transitional and fully turbulent) had significantly different boundary layer profiles compared to experiments (Fig. 16a). To enable a quantitative assessment and comparison with the experiments, the computations were sampled at the same location as the LDA measurements and the streamwise velocity profiles were fitted through a Sun and Child model [35] of the log and wake region to determine the outer edge velocity and thickness of the boundary layers. This approach is typically used in experiments to reduce the uncertainty on the computations of the boundary layer integral quantities [36] due to the lack of near wall spatial resolution, and it relies on the assumptions of adiabatic flow conditions and equilibrium turbulent boundary layer. For the attached and incipient separation cases ($h_{bump}/\Delta y_{rig,in} = 0.159$ and 0.194), the first assumption holds given that there was no notable flow unsteadiness observed in the experiments. The equilibrium boundary layer assumption was verified through the use of the CFD data and it is further discussed in the next sections. The linearity between the raw data and the model prediction was evaluated through the Pearson coefficient. The average Pearson coefficient for the fitted data (experimental and CFD) was typically above 98%. Compared to experiments, the boundary layer at $\Delta x/L_{nac} \approx 0.06$ for the case with incipient separation ($h_{bump}/\Delta y_{rig,in} = 0.194$)

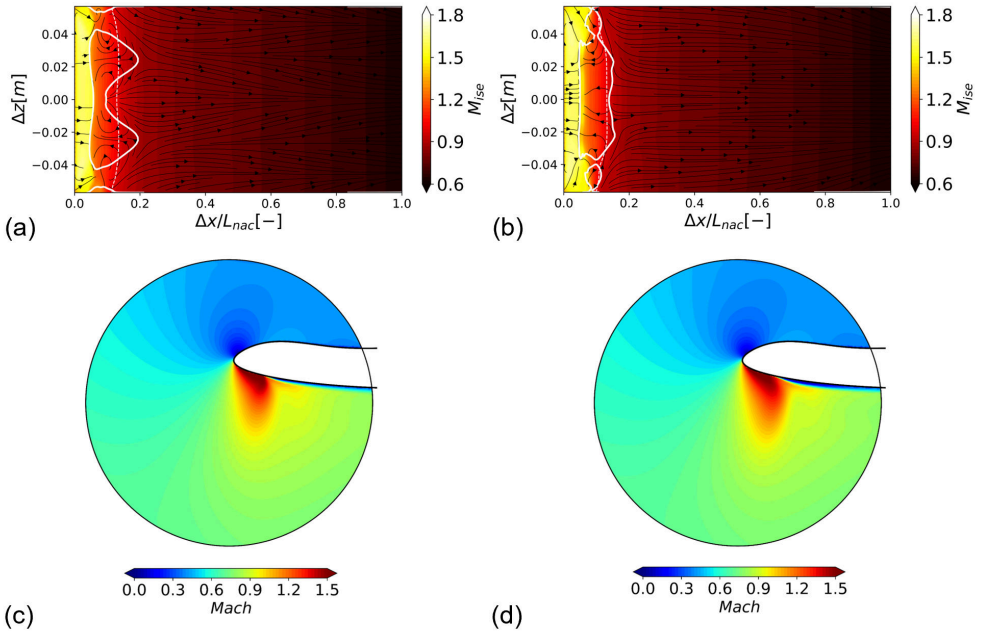

Fig. 15 a), b) M_{ise} distribution on the nacelle aeroline; white solid line: $\tau_{w,x} = 0$; white dashed line: $M_{ise} = 1$. b), c) Mach number distribution at $\Delta z = 0$. $h_{bump}/\Delta y_{rig,in} = 0.227$ and $M_{in} = 0.65$. RANS with a), c) and b), d) $\gamma - Re_\theta$ turbulence models

was about 25% and 15% thicker for the fully turbulent ($k\omega - SST$) and transitional ($\gamma - Re_\theta$) models, respectively (Fig. 16a). The similarities between the two turbulence models were also confirmed by the production of turbulent kinetic energy (G_k, Fig. 16b) across the velocity profile, which was only slightly different in the core flow region. Further downstream of the shock ($\Delta x/L_{nac} \approx 0.13$), the two models had similar boundary layer profiles with a thickness that was about 30% and 20% greater compared to experiments for the attached ($h_{bump}/\Delta y_{rig,in} = 0.159$) and incipient separation ($h_{bump}/\Delta y_{rig,in} = 0.194$) cases, respectively (Fig. 17).

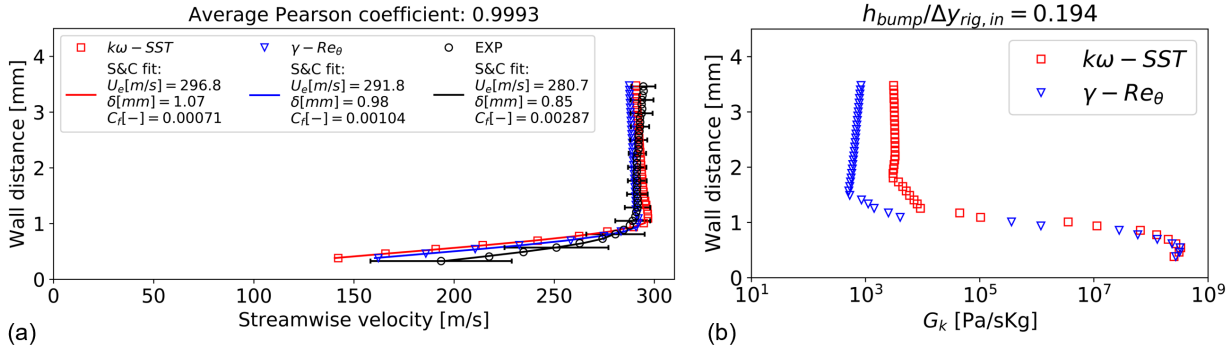

Fig. 16 a) Streamwise velocity and b) modelled G_k on the nacelle aeroline at $\Delta x/L_{nac} \approx 0.06$ and $\Delta z = 0$. $h_{bump}/\Delta y_{rig,in} = 0.194$ and $M_{in} = 0.65$. Solid lines: Sun and Child ($S\&C$) boundary layer fit. Error bars on the experimental data are only displayed every 3^{rd} point for readability

For the case with a well-established boundary layer separation ($h_{bump}/\Delta y_{rig,in} = 0.227$), the differences in the

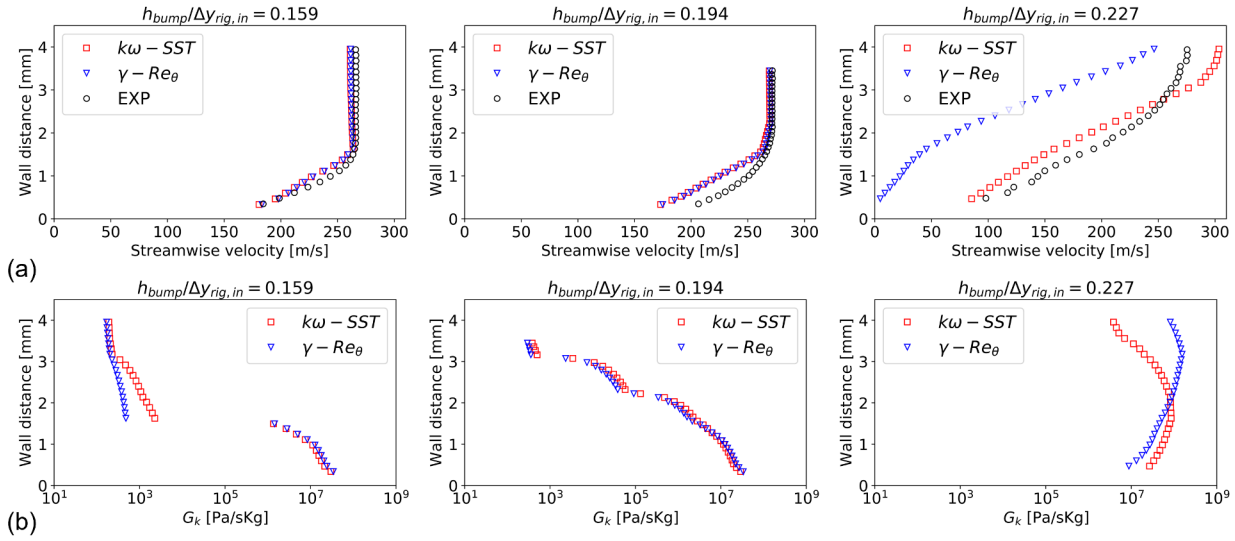

Fig. 17 a) Streamwise velocity and b) modelled G_k distributions on the nacelle aeroline at $\Delta x/L_{nac} \approx 0.13$ and $\Delta z = 0$. Experimental error bars not displayed for readability

boundary layer were considerable (Fig. 17) both relative to the experiments, but also between the two turbulence models. The transitional model ($\gamma - Re_\theta$) was separated at $\Delta x/L_{nac} \approx 0.13$ (Fig. 15b) and the peak in G_k was further away from the wall relative to the results from the fully turbulent ($k\omega - SST$) model (Fig. 17b) due to the presence of the separated shear layer. Although at $\Delta x/L_{nac} \approx 0.13$ there was no separation for the fully turbulent computations and for the experiments, the boundary layer was far from an equilibrium state. This could be inferred from the analysis of the axial distribution of the integral characteristics of the boundary layer for the two CFD models (transitional and fully turbulent, Fig. 18). The near-wall resolution of the computational models both ahead and downstream of the shock was exploited to compute the compressible (H_c) and incompressible (H_i) shape factors of the boundary layer as well the Rotta-Clauser parameter (β). The methodology followed for the computations of the integral quantities was introduced in section II.A.1. Ahead of the shock ($\Delta x/L_{nac} \approx 0.015$), for the transitional computations ($\gamma - Re_\theta$) the boundary layer (Fig. 19a) was almost fully laminar with an incompressible shape factor $H_i \approx 2.5$ (Fig. 18b). This was similar to the Prandtl value of $H_i = 2.56$ for an incompressible laminar boundary layer over a flat plate with no pressure gradient, despite the presence of a notable favourable pressure gradient indicated by the negative values of β in Fig. 18. For the transitional computations ($\gamma - Re_\theta$), the status of the boundary layer ahead of the shock was also confirmed by the intermittency below 1 (Fig. 19b) and from the value of turbulent kinetic energy (TKE, Fig. 19c) which was about 3 orders of magnitude lower compared to a boundary layer at an axial position further downstream of the shock ($\Delta x/L_{nac} \approx 0.42$).

For the attached ($h_{bump}/\Delta y_{rig,in} = 0.159$) and incipient separation cases ($h_{bump}/\Delta y_{rig,in} = 0.194$), H_i after the shock ($\Delta x/L_{nac} > 0.25$) reduced to approximately $H_i \approx 1.4$ for both the transitional and fully turbulent model (Fig.

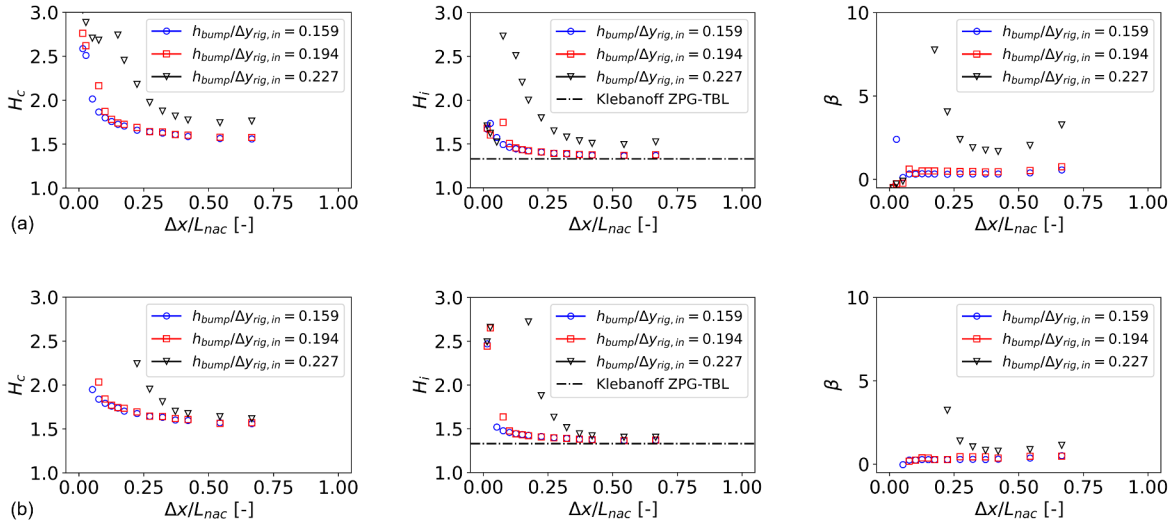

Fig. 18 Boundary layer characteristics on the nacelle aeroline at $\Delta z = 0$. RANS with a) $k\omega - SST$ and b) $\gamma - Re_\theta$ turbulence models

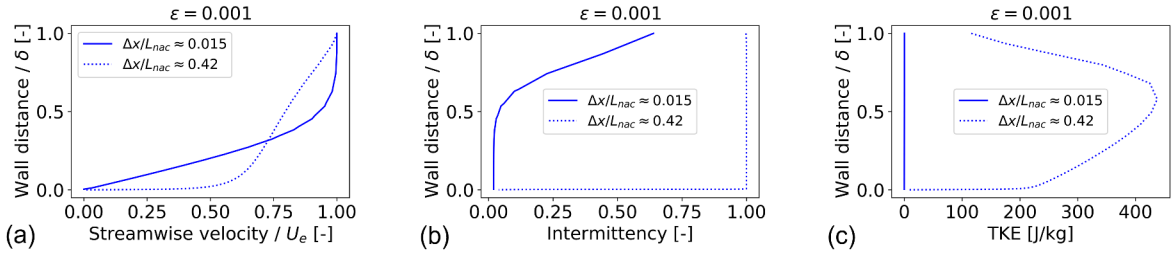

Fig. 19 a) Non-dimensional streamwise velocity, b) intermittency and c) turbulent kinetic energy distributions across the boundary layer on the nacelle aeroline at $\Delta z = 0$. $h_{bump}/\Delta y_{rig,in} = 0.227$. RANS with $\gamma - Re_\theta$ turbulence model

18). The value is close to a typical value for an incompressible equilibrium turbulent boundary layer with zero pressure gradient (ZPG-TBL, [37]) and it indicated that the mean flow profile of the boundary layer fully recovered after the shock. The Rotta-Clauser parameter (β) between $\Delta x/L_{nac} \approx 0.2$ and 0.7 was approximately constant for both models (Fig. 18) at about $\beta \approx 0.3$ and $\beta \approx 0.45$ for the attached and incipient separation case, respectively. This indicated that the boundary layer for both bump configurations had reached an equilibrium state. This conclusion was further corroborated by rescaling the boundary layers in wall units (Fig. 20). Across the range of approximately constant β, the boundary layer profiles for the fully turbulent case ($k\omega - SST$, Fig. 20a) were almost independent of the axial position. The minor differences within the viscous sub-region ($y^+ < 5$) were due to an increase in the friction length under the influence of the adverse pressure gradient on the afterbody of the nacelle aeroline and a consequent reduction of the first cell y^+. For the transitional case ($\gamma - Re_\theta$, Fig. 20b), the configuration with incipient separation ($h_{bump}/\Delta y_{rig,in} = 0.194$) had slightly different profiles at $\Delta x/L_{nac} \approx 0.22$ compared to 0.54 and 0.67. This may be an indication of a slightly

reduced recovery region for the case with transitional interaction. Overall, for the attached ($h_{bump}/\Delta y_{rig,in} = 0.159$) and incipient separation ($h_{bump}/\Delta y_{rig,in} = 0.194$) cases, the recovery length of the boundary layer in the CFD model was only slightly affected by the nature (fully turbulent or transitional) of the SBLI. This was similarly observed in an experiment in a different rig configuration [10] where the influence of the nature of the interaction between the shock and the boundary layer was assessed through a change in Reynolds number.

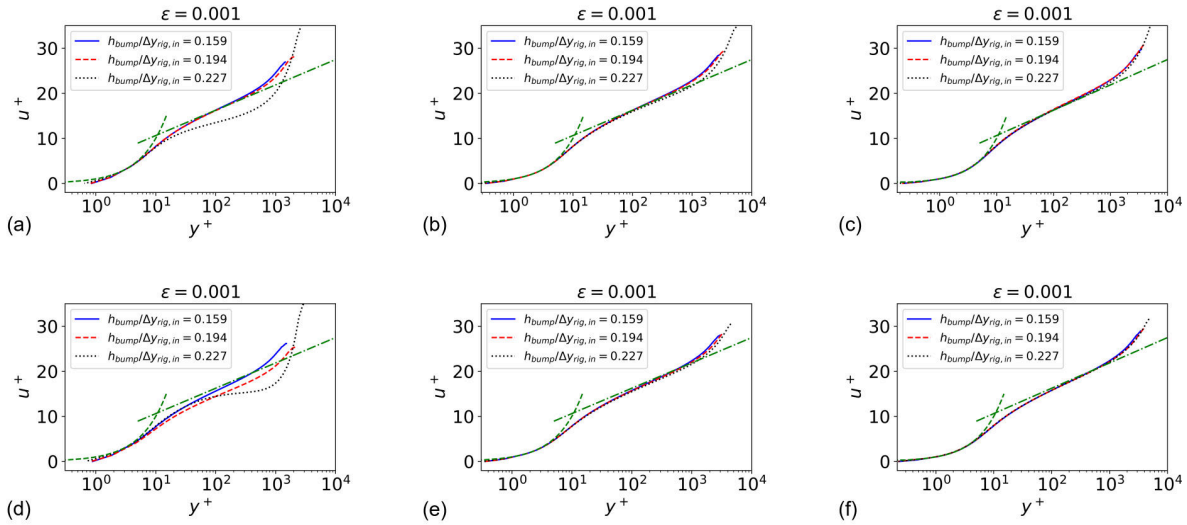

Fig. 20 Boundary layers on the nacelle aeroline at $\Delta z = 0$. RANS with a) $k\omega - SST$ and b) $\gamma - Re_\theta$ turbulence models. Green dashed line: linear region ($u^+ = y^+$); dotted-dashed green line: log region ($u^+ = \frac{1}{0.41} ln(y^+) + 5.0$)

For the configuration with a well-established separation ($h_{bump}/\Delta y_{rig,in} = 0.227$), the characteristics of the boundary layer downstream of the shock were significantly different for the transitional ($\gamma - Re_\theta$) and fully turbulent ($k\omega - SST$) models. However, this was expected given the notable changes in spanwise and streamwise distribution of the separated region (Fig 15). For the transitional model, the boundary layer almost recovered to a healthy ($H_i(x) \approx 1.3 - 1.4$, [38]) turbulent boundary layer with $H_i \approx 1.45$, whereas H_i was greater ($H_i \approx 1.6$) for the fully turbulent case. The streamwise distribution of β was significantly different for the two CFD models. The transitional model reached an almost equilibrium turbulent boundary layer at $\Delta x/L_{nac} \approx 0.5 - 0.6$ (Fig. 18b), despite a more pronounced wake region ($y^+ > 10^3$, Fig. 20) compared to the attached ($h_{bump}/\Delta y_{rig,in} = 0.159$) and incipient separation ($h_{bump}/\Delta y_{rig,in} = 0.194$) cases. On the other hand, the boundary layer for the fully turbulent model did not reach an equilibrium state with the β parameter that decreased in the post-shock region ($0.2 < \Delta x/L_{nac} < 0.6$) and then increased again under the influence of the adverse pressure gradient in the afterbody part of the nacelle cowl ($\Delta x/L_{nac} > 0.6$, Fig. 18a). However, for this configuration ($h_{bump}/\Delta y_{rig,in} = 0.227$), due to the considerable differences between the CFD and the experiments, it is argued that the characteristics of the SBLI at mid-span ($\Delta z = 0$) in the CFD models were significantly affected by a different prediction of the topology of the corner flows for the two

turbulence models.

Overall, at the nominal inlet Mach number ($M_{in} = 0.65$), both turbulence models captured the separation onset of the boundary layer on the nacelle cowl due to changes in bump height, i.e. MFCR. Within an industrial design framework where the separation onset of the boundary layer can be a criterion [2, 39] to establish the viability of the design, steady RANS methods proved sufficiently accurate when compared to experiments. For this configuration, the transitional ($\gamma - Re_\theta$) model had a better agreement with the experiments relative to the shock characteristics. Nevertheless, both CFD models failed to predict the reattachment point and the recovery of the boundary layer for the case with a well-established separation. In the next section the sensitivity of the boundary layer to changes in inlet Mach number is also assessed and the sensitivity of post-shock boundary layer characteristics to changes in pre-shock Mach number and post-shock diffusion determined.

1. Effect of inlet Mach number and MFCR on SBLI

The inlet Mach number within the rig was reduced to $M_{in} = 0.60$ with the operating total pressure and temperature held constant. The shock characteristics for both experimental and CFD data were determined as explained in section II.A.1 and the sensitivity to changes in inlet Mach number was also assessed. To overcome the reduced spatial resolution for the experimental data compared to the CFD, the pressure taps measurements were fitted through a spline curve to determine the pre-shock and the sonic axial position (Fig. 3). For consistency, the same approach was also adopted for the CFD data. For both inlet conditions ($M_{in} = 0.6, 0.65$), the transitional ($\gamma - Re_\theta$) model had a better agreement with the experiments compared to the fully turbulent case ($k\omega - SST$) in terms of pre-shock Mach number (Fig. 21a) with a difference that was less than 0.05 across the changes in inlet Mach number and mass flow split, i.e. MFCR. The same was generally true relative to the shock strength (PR_{sw}, Fig. 21b). For the configuration $h_{bump}/\Delta y_{rig,in} = 0.227$, both models significantly under-predicted the strength of the shock. Nevertheless, as discussed in the previous section, it is believed that at the higher inlet Mach number ($M_{in} = 0.65$) the CFD prediction of the corner flows had a dominant role for the configuration with the more aggressive change in MFCR, which significantly affected the interaction between the shock and the boundary layer and the comparison with the experiments.

The presence of shock-induced boundary layer separation is typically a function of pre-shock Mach number and the status of the boundary layer ahead of the shock [40]. For a nacelle under windmilling diversion conditions, the presence of a notable favourable pressure-gradient due to the acceleration around the nacelle leading edge and the post-shock diffusion can significantly affect the characteristics of the SBLI. Thus, the likely correlation between the presence of shock-induced boundary layer separation, pre-shock Mach number ($M_{ise,pre-sw}$), favourable pressure gradient (β_{pre-sw}) and incompressible shape factor ($H_{i,pre-sw}$ at $\Delta x/L_{nac} \approx 0.015$, Fig. 22a) was evaluated along with the recovery of the post-shock boundary layer. The latter was quantified based on the average incompressible shape factor

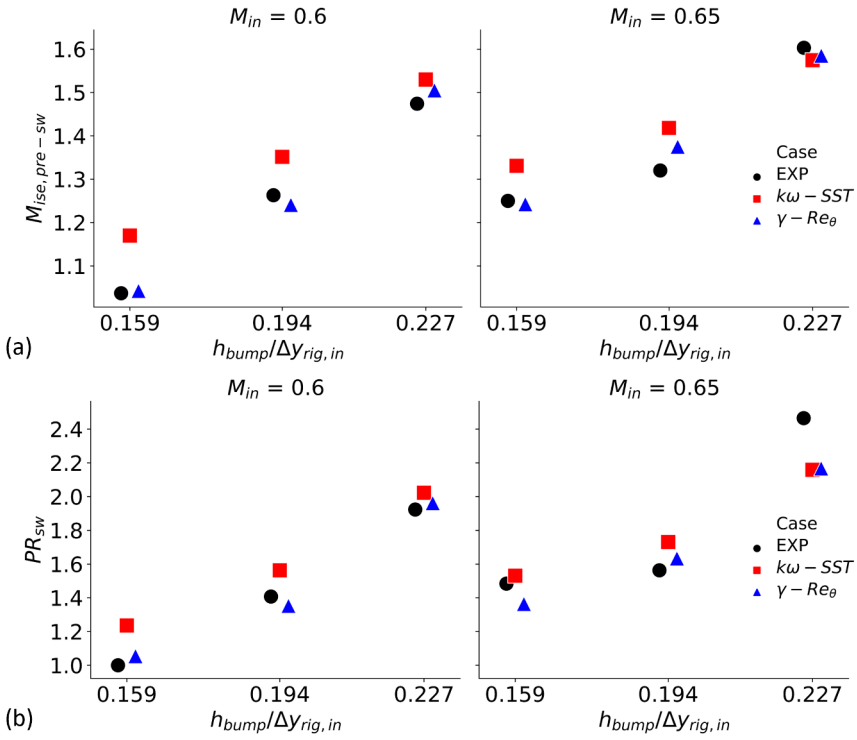

Fig. 21 Effect of change in bump height on a) pre-shock isentropic Mach number and b) shock strength

($\overline{H_{i,eq}}$) in the equilibrium region ($\Delta x/L_{nac} \approx 0.2$ and 0.6, Fig. 22a). The lowest pre-shock Mach number that promotes turbulent boundary layer separation is here referred to as a critical pre-shock Mach number. For the fully turbulent ($k\omega - SST$) computations this was around 1.42 with $H_{i,pre-sw} \approx 1.65$, whereas the transitional model ($\gamma - Re_\theta$) had $M_{ise,pre-sw} \approx 1.38$ (Fig. 22b) with a greater incompressible shape factor ahead of the shock ($H_{i,pre-sw} \approx 2.5$) associated to a laminar boundary layer, although this was either transitional or fully turbulent at the axial position of the interaction with the shock. For the fully turbulent model ($k\omega - SST$), the shape factor was significantly greater than the data available in the open literature (Fig. 22a, [40]). Compared to previous work, in this configuration the boundary layer ahead of the shock was far from an equilibrium state due to the notable favourable pressure gradient around the nacelle leading edge ($\beta_{pre-sw} \approx -1.0$, Fig. 22b) associated with the flow streamwise acceleration. For $M_{ise,pre-sw} \approx 1.4$, despite the presence of shock induced separation for both CFD models (transitional and fully turbulent), the boundary layer downstream of the shock recovered ($\overline{H_{i,eq}} \approx 1.4$, Fig. 22c). As the pre-shock Mach number increased to about $1.5 - 1.55$, the boundary layer was still able to recover and it reached an equilibrium status (Fig. 18), despite a slight increase in incompressible shape factor (Fig. 22c). A further increase in pre-shock Mach number ($M_{ise,pre-sw} \approx 1.6$) significantly increased the average shape factor in the post-shock region, with the boundary layer that did not reach an equilibrium state for the fully turbulent computations as explained in the previous section. Overall, based on the validated CFD data, the critical pre-shock Mach number associated with incipient separation

was about $M_{ise,pre-sw} \approx 1.4$, which is slightly higher compared to previous work [40]. This is depicted in Figure 22 where the solid and dashed lines are based on Delery (1985) [40] and they mark separated (above) and attached (below) boundary layer regions. However, a key consideration is the 'effective' aspect ratio of the rig [41] which also needs to be evaluated.

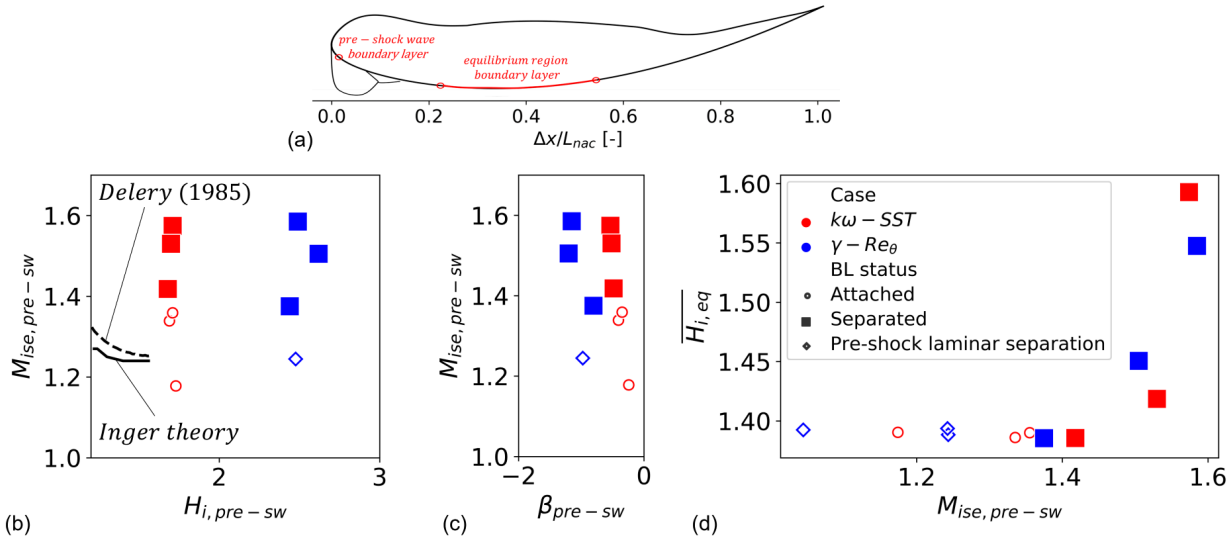

Fig. 22 a) Schematic of axial position of pre-sock and equilibrium boundary layers; b), c), d) correlations between pre-shock Mach number and boundary layer characteristics

The two-dimensionality of the interaction between the shock and the boundary layer at the tunnel mid-span ($\Delta z = 0$) is typically evaluated through an 'effective' aspect ratio ($\frac{\delta^*_{i,pre-sw}}{\Delta z_{rig}}$, [41]) of the experimental facility, which is defined as the ratio between the incompressible displacement thickness of the boundary layer ahead of the shock ($\delta^*_{i,pre-sw}$) at the center-line and the tunnel width (Δz_{rig}). For a nominally two-dimensional experiment, $\frac{\delta^*_{i,pre-sw}}{\Delta z_{rig}}$ is close to zero and it increases with an increase in the confinement of the experiments due to the small size of the facility relative to the boundary layer thickness. It was shown that this parameters significantly influences the value of the pre-shock Mach number that causes boundary layer separation. For the configuration investigated in this work $\frac{\delta^*_{i,pre-sw}}{\Delta z_{rig}}$ was about $0.25 - 0.3 \times 10^3$. Based on previous work [41], the onset of boundary layer separation is expected for a pre-shock Mach number of $M_{ise,pre-sw} \approx 1.35$. For the fully turbulent computations ($k\omega - SST$) there were two attached point above the dashed line in Figure 23, which marks separated (above) and attached (below) boundary layer regions based on a collection of experimental data in the open literature. Nevertheless, it was previously shown (Fig. 21) that for the configuration presented in this work, the fully turbulent computations overestimated the pre-shock Mach number compared to the experiments. On the other hand, the transitional ($\gamma - Re_\theta$) model closely matched the experimental critical pre-shock Mach number for a range of MFCR and M_{in} (Fig. 21). Both experiments and the transitional ($\gamma - Re_\theta$) computations generally agreed with the data in the literature relative to the effect of pre-shock Mach number on shock-induced boundary layer separation (Fig. 23).

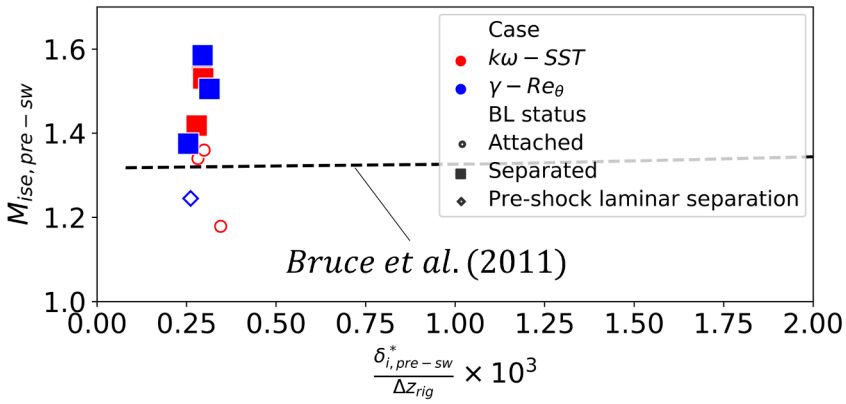

Fig. 23 Effect of tunnel blockage on 'critical' pre-shock Mach number

IV. Conclusion

This work assessed the limitation of steady RANS CFD methods based on fully turbulent and transitional turbulence models for the assessment of the separation onset and characteristics of the boundary layer on a rig configuration which is representative of the aerodynamics of compact aero-engine nacelles under windmilling conditions. From a nacelle industrial design optimisation point of view which aims to maximize fuel burn savings while also avoiding separation under off-design conditions, steady RANS methods proved sufficiently accurate to capture the separation onset of the boundary layer on the nacelle cowl under windmilling diversion conditions.

The correlation between incipient boundary layer separation and pre-shock Mach number was also evaluated for a range of inlet Mach number and MFCR. The critical pre-shock Mach number was about 1.4, which was slightly greater compared to previous experimental studies for SBLI when the effective aspect ratio of the rig is also taken into account. Based on the validated CFD data, the characteristics of the boundary layer ahead and downstream of the shock were also determined. The recovery of the boundary layer was not significantly affected by the characteristics (transitional or fully turbulent) of the SBLI. The work showed that when the pre-shock Mach number increased to about 1.55, the boundary layer reattached after the shock and it was able to reach an equilibrium state with an incompressible shape factor of about 1.45. With a further increase in shock strength ($M_{ise,pre-sw} \approx 1.6$), the boundary layer reattached after the shock, but, based on the fully turbulent computations, it was not able to reach an equilibrium state. Overall, the work provides guidance on the critical pre-shock Mach number that may be tolerable within a design framework for a configuration that exhibit similar pre-shock boundary layer characteristics and interactions with a near-normal shock wave.

Acknowledgments

This project has received funding from the Clean Sky 2 Joint Undertaking (JU) under grant agreement number 101007598. The JU receives support from the European Union's Horizon 2020 research and innovation programme and

the Clean Sky 2 JU members other than the Union. The authors would like to thank Connor O'Pray (Rolls-Royce plc) for his help with the final draft of the manuscript.

Data availability statement

Due to commercial confidentiality agreements the supporting data are not available.

References

[1] Anon, "Estimation of drag due to inoperative turbo-jet and turbo-fan engines," *Engineering Sciences Data Unit, Data Items*, , No. ESDU 81009, 1984.

[2] Hoelmer, W., Younghans, J. L., and Raynal, J. C., "Effect of Reynolds number on upper cowl flow separation," *Journal of Aircraft*, Vol. 24, No. 3, 1987, pp. 161–169. https://doi.org/10.2514/3.45411.

[3] Deneys Schreiner, B. J., Tejero, F., MacManus, D. G., and Sheaf, C., "Robust aerodynamic design of nacelles for future civil aero-engines," *Proceedings of the ASME Turbo Expo*, Vol. 1, No. M, 2020, pp. 1–11. https://doi.org/10.1115/GT2020-14470.

[4] Swarthout, A., MacManus, D., Tejero, F., Matesanz-García, J., Boscagli, L., and Sheaf, C., "A comparative assessment of multi-objective optimisation methodologies for aero-engine nacelles," *ICAS September 2022*, 2022, p. 0162.

[5] Sánchez Moreno, F., MacManus, D., Hueso Rebassa, J., Tejero, F., and Sheaf, C., "Optimization of installed compact and robust nacelles using surrogate models," *ICAS September 2022*, 2022, p. 0159.

[6] Kalsi, H. S., and Tucker, P. G., *Numerical modelling of shock wave boundary layer interactions in aero-engine intakes at incidence*, Vol. 50985, American Society of Mechanical Engineers, 2018.

[7] Oriji, U. R., and Tucker, P. G., "Modular Turbulence Modeling Applied to an Engine Intake," *Journal of Turbomachinery*, Vol. 136, No. 5, 2013. https://doi.org/10.1115/1.4025232, URL https://doi.org/10.1115/1.4025232, 051004.

[8] Boscagli, L., Tejero, F., Swarthout, A. E., MacManus, D. G., Sabnis, K., Babinsky, H., and Sheaf, C., "Design of a quasi-2D rig configuration to assess nacelle aerodynamics under windmilling conditions," *AIAA AVIATION 2023 Forum*, 2023, p. 3392. https://doi.org/10.2514/6.2023-3392.

[9] Sabnis, K., Boscagli, L., Swarthout, A., Tejero Embuena, F., Babinsky, H., David, M., and Sheaf, C., "A Wind Tunnel Rig to Study the External Fan Cowl Separation Experienced by Compact Nacelles in Windmilling Scenarios," *AIAA Scitech 2023 Forum*, 2023, p. 1942. https://doi.org/10.2514/6.2023-1942.

[10] Coschignano, A., Atkins, N., Babinsky, H., and Serna, J., "Effect of Reynolds number on a normal shock wave-transitional boundary-layer interaction over a curved surface," *Experiments in Fluids*, Vol. 60, No. 12, 2019, pp. 1–12. https://doi.org/10.1007/s00348-019-2824-0, URL https://doi.org/10.1007/s00348-019-2824-0.

[11] Coschignano, A., and Babinsky, H., "Boundary-Layer Development Downstream of Normal Shock in Transonic Intakes at Incidence," *AIAA Journal*, Vol. 57, No. 12, 2019, pp. 5241–5251. https://doi.org/10.2514/1.j058508.

[12] Tejero, F., Christie, R., MacManus, D., and Sheaf, C., "Non-axisymmetric aero-engine nacelle design by surrogate-based methods," *Aerospace Science and Technology*, Vol. 117, 2021, p. 106890. https://doi.org/10.1016/j.ast.2021.106890, URL https://doi.org/10.1016/j.ast.2021.106890.

[13] ANSYS Inc, "ANSYS FLUENT User's Guide," Tech. rep., Canonsburg, PA 15317, 2019.

[14] Menter, F. R., Kuntz, M., and Langtry, R., "Ten years of industrial experience with the SST turbulence model," *Turbulence, heat and mass transfer*, Vol. 4, No. 1, 2003, pp. 625–632.

[15] Menter, F. R., Langtry, R. B., Likki, S., Suzen, Y., Huang, P., and Völker, S., "A correlation-based transition model using local variables—part I: model formulation," *Journal of turbomachinery*, Vol. 128, No. 3, 2006, pp. 413–422.

[16] Jones, W. P., and Launder, B., "Some properties of sink-flow turbulent boundary layers," *Journal of Fluid Mechanics*, Vol. 56, No. 2, 1972, pp. 337–351.

[17] Piomelli, U., Balaras, E., and Pascarelli, A., "Turbulent structures in accelerating boundary layers," *Journal of Turbulence*, Vol. 1, No. 1, 2000, p. 001.

[18] Jones, W. P., and Launder, B. E., "The prediction of laminarization with a two-equation model of turbulence," *International journal of heat and mass transfer*, Vol. 15, No. 2, 1972, pp. 301–314.

[19] Mayle, R. E., "The 1991 IGTI Scholar Lecture: The Role of Laminar-Turbulent Transition in Gas Turbine Engines," *Journal of Turbomachinery*, Vol. 113, No. 4, 1991, pp. 509–536. https://doi.org/10.1115/1.2929110, URL https://doi.org/10.1115/1.2929110.

[20] Clauser, F. H., "Turbulent boundary layers in adverse pressure gradients," *Journal of the Aeronautical Sciences*, Vol. 21, No. 2, 1954, pp. 91–108.

[21] Vinuesa, R., Negi, P. S., Atzori, M., Hanifi, A., Henningson, D. S., and Schlatter, P., "Turbulent boundary layers around wing sections up to Rec= 1,000,000," *International Journal of Heat and Fluid Flow*, Vol. 72, 2018, pp. 86–99.

[22] Schlichting, H., and Gersten, K., *Boundary-layer theory*, Springer Science & Business Media, 2003.

[23] Schetz, J. A., and Bowersox, R. D. W., *Boundary layer analysis*, American Institute of Aeronautics and Astronautics, 2011.

[24] Morkovin, M. V., "Effects of compressibility on turbulent flows," *Mécanique de la Turbulence*, Vol. 367, No. 380, 1962, p. 26.

[25] Celik, I. B., Ghia, U., Roache, P. J., Freitas, C. J., Coleman, H., and Raad, P. E., "Procedure for estimation and reporting of uncertainty due to discretization in CFD applications," *Journal of Fluids Engineering, Transactions of the ASME*, Vol. 130, No. 7, 2008, pp. 0780011–0780014. https://doi.org/10.1115/1.2960953.

[26] Bruce, P., Babinsky, H., Tartinville, B., and Hirsch, C., "Corner effect and asymmetry in transonic channel flows," *AIAA journal*, Vol. 49, No. 11, 2011, pp. 2382–2392.

[27] Spalart, P. R., "Strategies for turbulence modelling and simulations," *International journal of heat and fluid flow*, Vol. 21, No. 3, 2000, pp. 252–263.

[28] Sabnis, K., Galbraith, D., Babinsky, H., and Benek, J. A., "Experimental validation of the quadratic constitutive relation in supersonic streamwise corner flows," *AIAA Scitech 2021 Forum*, 2021, p. 1740.

[29] Spalart, P. R., and Allmaras, S. R., "One-equation turbulence model for aerodynamic flows," *Recherche aerospatiale*, , No. 1, 1994, pp. 5–21. https://doi.org/10.2514/6.1992-439.

[30] Goulos, I., Otter, J., Tejero, F., Hueso Rebassa, J., MacManus, D., and Sheaf, C., "Civil turbofan propulsion aerodynamics: Thrust-drag accounting and impact of engine installation position," *Aerospace Science and Technology*, Vol. 111, 2021, p. 106533. https://doi.org/10.1016/j.ast.2021.106533, URL https://doi.org/10.1016/j.ast.2021.106533.

[31] O'Pray, C. E., Babinsky, H., and Sheaf, C., "The Influence of Surface Geometry on the Fan-Plane Boundary-Layer in Transonic Intakes at High-Incidence," *AIAA SCITECH 2022 Forum*, 2022, p. 1806.

[32] Sabnis, K., Boscagli, L., Babinsky, H., MacManus, D. G., and Sheaf, C., "Experimental Investigation of External Fan Cowl Separation for Compact Nacelles in Windmilling Scenarios," *AIAA AVIATION 2023 Forum*, 2023, p. 3394. https://doi.org/10.2514/6.2023-3394.

[33] Cabral, B., and Leedom, L. C., "Imaging Vector Fields Using Line Integral Convolution," *Proceedings of the 20th Annual Conference on Computer Graphics and Interactive Techniques*, Association for Computing Machinery, New York, NY, USA, 1993, p. 263–270. https://doi.org/10.1145/166117.166151, URL https://doi.org/10.1145/166117.166151.

[34] Van Driest, E. R., *The problem of aerodynamic heating*, Institute of the Aeronautical Sciences, 1956.

[35] Sun, C.-C., and Childs, M. E., "A modified wall wake velocity profile for turbulent compressible boundary layers." *Journal of Aircraft*, Vol. 10, No. 6, 1973, pp. 381–383.

[36] Titchener, N., Colliss, S., and Babinsky, H., "On the calculation of boundary-layer parameters from discrete data," *Experiments in Fluids*, Vol. 56, 2015, pp. 1–18.

[37] Klebanoff, P., "Characteristics of turbulence in a boundary layer with zero pressure gradient," Tech. rep., National Bureau of Standards Gaithersburg Md, 1955.

[38] Anderson, B., Tinapple, J., and Surber, L., "Optimal control of shock wave turbulent boundary layer interactions using micro-array actuation," *3rd AIAA flow control conference*, 2006, p. 3197. https://doi.org/10.2514/6.2006-3197.

[39] Motycka, D. L., "Reynolds number and fan/inlet coupling effects on subsonic transport inlet distortion," *Journal of Propulsion and Power*, Vol. 1, No. 3, 1985, pp. 229–234. https://doi.org/10.2514/3.22785.

[40] Delery, J. M., "Shock wave/turbulent boundary layer interaction and its control," *Progress in Aerospace Sciences*, Vol. 22, No. 4, 1985, pp. 209–280.

[41] Bruce, P., Burton, D., Titchener, N., and Babinsky, H., "Corner effect and separation in transonic channel flows," *Journal of Fluid Mechanics*, Vol. 679, 2011, pp. 247–262.

2023-11-02

Characteristics of shock-induced boundary-layer separation on nacelles under windmilling diversion conditions

Boscagli, Luca

AIAA

Boscagli L, MacManus D, Tejero F, et al., (2024) Characteristics of shock-induced boundary-layer separation on nacelles under windmilling diversion conditions. AIAA Journal, Volume 62, Issue 1, January 2024, pp. 79-91

https://doi.org/10.2514/1.J063209